

CORONAVIRUS

Femtomolar detection of SARS-CoV-2 via peptide beacons integrated on a miniaturized TIRF microscope

Soumya P. Tripathy^{1,2}, Manvitha Ponnappati^{1,2}, Suhaas Bhat³, Joseph Jacobson^{1,2}, Pranam Chatterjee^{1,2,3*}

The novel coronavirus SARS-CoV-2 (severe acute respiratory syndrome coronavirus 2) continues to pose a substantial global health threat. Along with vaccines and targeted therapeutics, there is a critical need for rapid diagnostic solutions. In this work, we use computational protein modeling tools to suggest molecular beacon architectures that function as conformational switches for high-sensitivity detection of the SARS-CoV-2 spike protein receptor binding domain (S-RBD). Integrating these beacons on a miniaturized total internal reflection fluorescence (mini-TIRF) microscope, we detect the S-RBD and pseudotyped SARS-CoV-2 with limits of detection in the femtomolar range. We envision that our designed mini-TIRF platform will serve as a robust platform for point-of-care diagnostics for SARS-CoV-2 and future emergent viral threats.

INTRODUCTION

As numerous countries are experiencing additional waves of coronavirus disease 2019 (COVID-19), rapid, point-of-care diagnostic tests enable triage of symptomatic individuals and control the outbreaks of the disease. The most widely used diagnostic tests for severe acute respiratory syndrome coronavirus 2 (SARS-CoV-2) are reverse transcription polymerase chain reaction (RT-PCR)-based methods (1), although other technologies based on CRISPR and loop-mediated amplification have been deployed as well (2–5). The best-in-class U.S. Food and Drug Administration (FDA)-authorized diagnostics, such as RT-PCR, have limits of detection (LoDs) of 10^2 to 10^3 RNA copies/ml, which is about 1 to 10 aM RNA in the test volume (6). RT-PCR tests, however, require laborious and expensive nucleic acid isolation, purification, and processing steps, which increase both the turnaround time of detection and the cost of testing (6, 7). Alternatively, there are FDA-authorized low-sensitivity, inexpensive, and rapid diagnostics. These tests, which often rely on antigen detection, have LoDs of 10^5 to 10^7 RNA copies/ml or around 1 to 100 fM (8).

Recently, there has been significant effort to detect SARS-CoV-2 via fluorescence-based readouts to allow for specific signal amplification (9–12). Such methods largely rely on binding to SARS-CoV-2 RNA or DNA, which requires isolation of nucleic acids, as described above. In this study, we first develop a molecular assay to detect the spike protein receptor binding domain (S-RBD) of SARS-CoV-2 using computationally validated peptide beacons, which enables single-step detection of S-RBD presence through the production of a fluorescence signal.

There are several reports on single molecular imaging and analysis using total internal reflection fluorescence (TIRF) microscopes (1, 13–21). TIRF microscopes deliver exquisite sensitivity by exciting fluorophores present within nanometer proximity of the device surface, producing high signal-to-background ratios (17, 22–24). There are several reports on miniaturized TIRF (mini-TIRF) microscope-based imaging and detection, where authors have used planar waveguide to create an evanescent field for exciting

surface-bound fluorophores (25–30). Adapting this technology, we fabricate a mini-TIRF microscope for seamless detection of beacon activity in response to viral presence, enabling rapid and highly sensitive detection of SARS-CoV-2.

RESULTS

Engineering of peptide beacon architecture

To construct a highly sensitive molecular beacon, we include two heterodimer-forming peptides, a binding ligand to the S-RBD, and a fluorophore-quencher pair at the terminal ends of the beacon (Fig. 1A). This fluorophore-quencher pair induces fluorescence quenching through the mechanism of Förster resonance energy transfer (FRET), where the efficiency of energy transfer between the fluorophore and quencher is proportional to the inverse sixth power of their spatial distance (31). Hence, a small change in spatial distance between the two beacon arms can drastically change the FRET efficiency, thus affecting the apparent fluorescent quantum yield of the fluorophore. Here, we used a commonly used fluorophore-quencher pair: fluorescein isothiocyanate (FITC) and [4-(N,N-dimethylamino)phenylazo] benzoyl, respectively. Upon binding to the target protein, the fluorophore

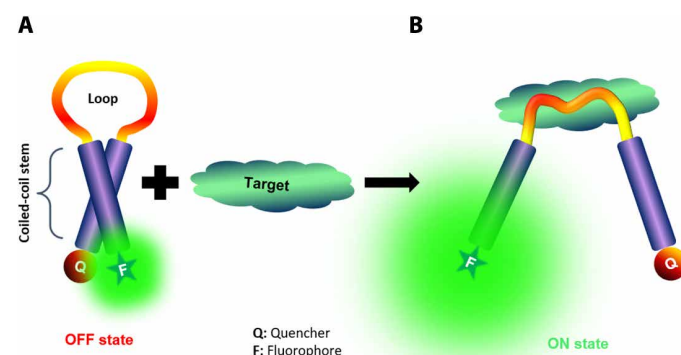


Fig. 1. Schematic of peptide beacon architecture. (A) Low-fluorescent state is the closed heterodimer state of the peptide beacon in the absence of S-RBD. (B) High-fluorescent state is the open-coil state after binding of S-RBD with the loop of the peptide beacon.

¹Center for Bits and Atoms, Massachusetts Institute of Technology, Cambridge, MA, USA. ²Media Lab, Massachusetts Institute of Technology, Cambridge, MA, USA. ³Department of Biomedical Engineering, Duke University, Durham, NC, USA. *Corresponding author. Email: pranam.chatterjee@duke.edu

and quencher are separated to observe an increase in fluorescence signal proportional to the amount of S-RBD present (Fig. 1B).

Computational examination of peptide beacon candidates

As a reference starting point for our designs, we used the coiled-coil peptide beacon architecture proposed by Mueller *et al.* (32). The reported peptide beacon designs consisted of the 21-mer conjugated with a binding ligand and one of the three peptides: C13, C17, and C21 (32). We designed our peptide beacons by replacing the binding portion of the sequences designed by Mueller *et al.* with our previously engineered 23-mer peptide that can bind to S-RBD and induce its degradation via the ubiquitin-proteasomal pathway (33).

To computationally examine whether insertion of our 23-mer peptide confers S-RBD binding, we folded and docked the three designs (C13LC21, C17LC21, and C21LC21) using trRosetta, Rosetta, and HDOCK (Fig. 2A) (34–36). Our results show that in the absence of S-RBD, all three peptides show terminal ends of the beacons, representing the fluorophore and the quencher, in close proximity to each other (OFF) in at least one of the top predicted models from trRosetta (34) or Rosetta Abinitio (Fig. 2, B and C) (35). When the C17LC21 and C21LC21 peptide beacon sequences

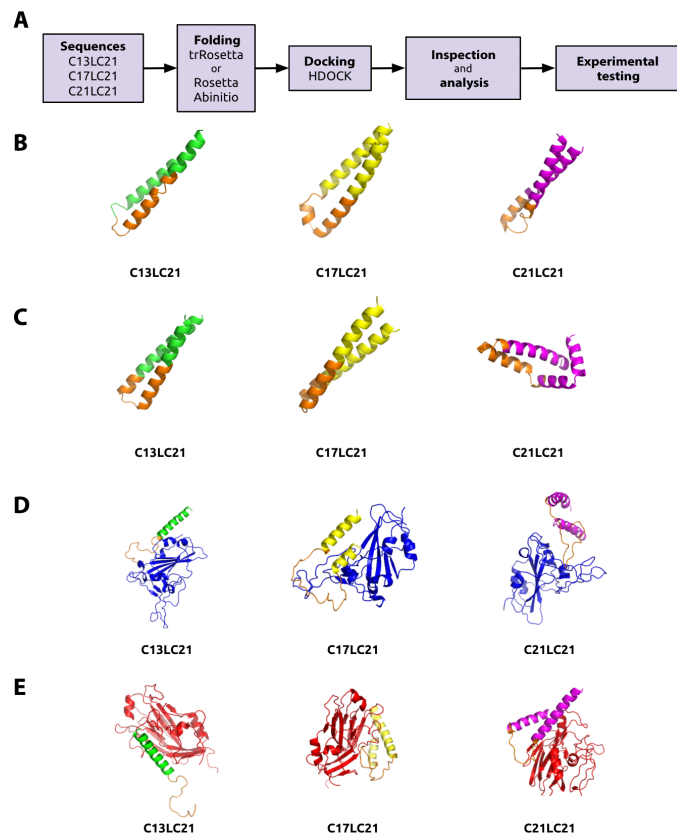


Fig. 2. In silico examination of peptide beacon architecture. (A) Computational pipeline. Sequences were folded ab initio via trRosetta or Rosetta Abinitio. The top structures were docked to S-RBD via HDOCK. Docked structures were analyzed, and candidate beacons were chosen. Highest-scoring (B) trRosetta structures, (C) Rosetta Abinitio structures, and (D) docked HDOCK structures of the three candidate beacons to S-RBD. The conserved binding peptide moiety is highlighted in orange. S-RBD is indicated in blue. (E) Docked HDOCK structures of the three candidate beacons to HA. The conserved binding peptide moiety is highlighted in orange. The HA protein is indicated in red.

were docked against S-RBD using the template-based hybrid docking software HDOCK (36), we observed the terminal ends to be spatially distanced from each other, indicating a possible ON state (Fig. 2D). This was in contrast to docking against the hemagglutinin protein of influenza A H3N2 (HA) negative control, where the peptide beacons did not form bound structures to the receptor (Fig. 2E) (37). As a note, the C13LC21 beacon did not form a complete docked structure for either S-RBD or HA, indicating a potential limitation of the pipeline. Thus, recognizing the inaccuracies of template-based docking tools, we sought to validate the three peptide designs via experimental testing.

Validation of S-RBD binding in human cells

To rapidly validate the binding capability of our peptide beacon designs, we adapted our previously described degradation assay in human cells, by fusing our peptide beacon candidates to the CHIPΔTPR E3 ubiquitin ligase, which can tag target proteins for degradation via the ubiquitin-proteasomal pathway in human cells (33). After cotransfection with a plasmid expressing S-RBD C-terminally fused to superfolder green fluorescent protein (sfGFP), we can measure binding affinity to S-RBD relative to sfGFP degradation. We tested various peptide beacon combinations, using our validated mutant S-RBD-binding peptide derived from angiotensin-converting enzyme 2 (ACE2), A2N (33), as well as a positive nanobody control, which has shown high affinity to S-RBD (38). As expected, these moieties alone demonstrate robust degradation capabilities, while the arms-only negative controls (C13, C17, C21, and C21*) show negligible degradation, hence no binding to the S-RBD. Of the complete peptide beacon constructs, the C17-A2N-C21* (C17LC21) beacon induces the greatest level of degradation of S-RBD-sfGFP, followed by C21LC21 and C13LC21, the latter of which exhibited minimal degradation capabilities (Fig. 3A).

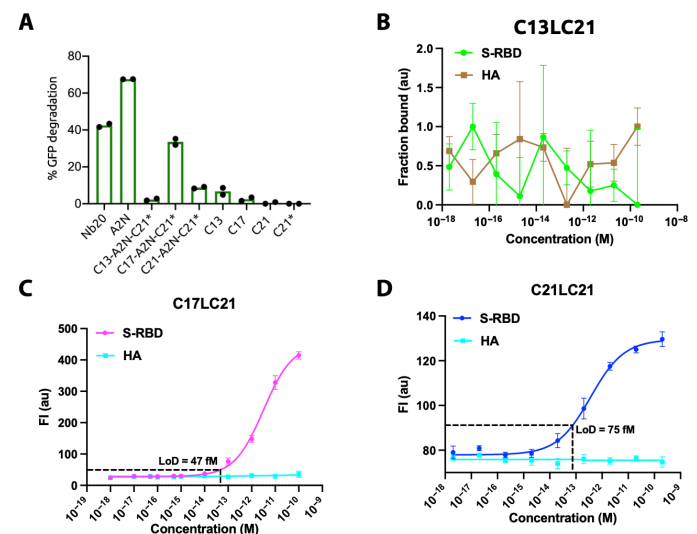


Fig. 3. Experimental characterization of peptide beacons. (A) Analysis of S-RBD-sfGFP degradation by flow cytometry. All samples were performed in independent transfection duplicates ($n = 2$) and gated on GFP⁺ fluorescence. Mean percentage of GFP⁺ cell depletion was calculated in comparison to the S-RBD-sfGFP-only control. C13LC21 is referred to as C13-A2N-C21*, C17LC21 is referred to as C17-A2N-C21*, and C21LC21 is referred to as C21-A2N-C21*. Titration of the target recombinant S-RBD and influenza H3N2 (HA) with 2 nM HPLC-purified (B) C13LC21 ($n = 3$), (C) C17LC21 ($n = 5$), and (D) C21LC21 ($n = 5$) in 1× PBS (pH 7.4). The LoD was calculated using Eq. 5. FI, fluorescence intensity; au, arbitrary units.

In vitro detection of S-RBD using peptide beacons

After ascertaining the binding capability of our candidates in human cells, we characterized the response of the peptide beacons in vitro in the presence of S-RBD. As a negative control, we also measured the cross-reactivity of our peptide beacons toward the HA protein (37). We first purified peptide beacons (CxxLC21) from the reaction mixture of CxxL + C21, using high-performance liquid chromatography (HPLC), and confirmed the presence of CxxLC21 in the collected fraction from HPLC through matrix-assisted laser desorption/ionization–time-of-flight (MALDI-TOF) mass spectrometry (fig. S1). We measured the fluorescent signals from the peptide beacons following a 10-min exposure to different concentrations of S-RBD and HA in 1× phosphate-buffered saline (PBS) and at pH 7.4 (Fig. 3, B to D). Of the three peptide beacons, C17LC21 showed the highest sensitivity toward S-RBD with an LoD of nearly 47 fM, followed by C21LC21 having an LoD of 75 fM. However, C13LC21 showed negligible response toward both S-RBD and HA. In conclusion, C17LC21 and C21LC21 can detect the presence of S-RBD with femtomolar sensitivity and low cross-reactivity, thus motivating their application for rapid detection of SARS-CoV-2.

Engineering of mini-TIRF device

To design a TIRF-based platform for the detection of fluorescent biomolecules, we first constructed a planar waveguide in which the glass core ($n_{\text{core}} = 1.53$) was fully coated with a low-refractive index polymer cladding ($n_{\text{cladding}} = 1.34$), except for a 1 mm by 1 mm area on a TIR spot to create a well for samples. The critical angle at the core-cladding interface was 61.142° for light having a wavelength of 488 nm. To create an evanescent field within the sample well, we coupled a collimated laser beam having a wavelength of 488 nm to

the planar waveguide at a coupling angle of 38° , which provides an angle of incidence of 66.272° , more than the critical angle of the core-cladding pair, at the core-cladding interface (Fig. 4A). After ascertaining the presence of an evanescent field on the mini-TIRF (movies S1 and S2), we characterized the performance of the device by measuring the fluorescence of surface-bound biotin-FITC in the sample well (Fig. 5A). Considering the fluorescent intensity of 1× PBS (pH 7.4) as a baseline control, we serially diluted biotin-FITC in 1× PBS (pH 7.4) and measured the fluorescence from the mini-TIRF following a 30-min exposure to different concentrations of biotin-FITC to the streptavidin-coated core surface within the sample well. Our fluorescence data suggest that the mini-TIRF can detect biotin-FITC with an LoD near 40 aM (Fig. 5B). In addition, a different cartridge has different background signals; hence, each cartridge requires individual calibration for the blank signal and LoD (Fig. 4G).

Detection of S-RBD and SARS-CoV-2 pseudovirus on the mini-TIRF

We next characterized the response of the beacon-immobilized mini-TIRF in the presence of S-RBD and virus pseudotyped with SARS-CoV-2 spike proteins, using the HA protein of influenza A H3N2 as the negative control. After purifying biotinylated peptide beacons (CxxLC21-Biotin) from the reaction mixture of CxxL + C21-Biotin using HPLC, we confirmed the presence of CxxLC21-Biotin in the collected fraction through MALDI-TOF mass spectrometry (fig. S2). We immobilized C17LC21-Biotin and C21LC21-Biotin on the mini-TIRF using an immobilized streptavidin layer and measured the fluorescent signals from the sensor following a 10-min exposure to different concentrations of S-RBD and HA in 1× PBS

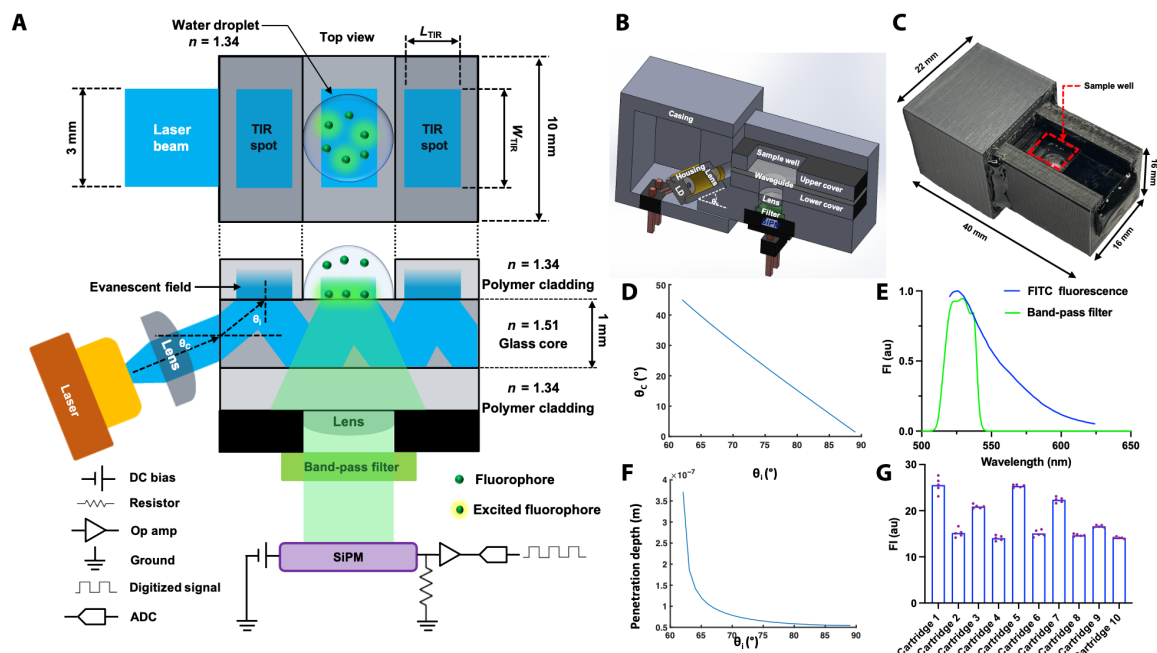


Fig. 4. Design of mini-TIRF. (A) Schematic showing the engineering of mini-TIRF device. ADC, analog-to-digital converter. (B) Internal architecture of the cartridge shown in a sliced solid work model. (C) Three-dimensional (3D)-printed cartridge containing a laser diode, planar waveguide, collimating lens, optical filter, and SiPM. (D) The graph between the angle of incidence that allows TIR and corresponding coupling angles. (E) Overlap between band-pass spectrum of the optical filter and emission spectrum of FITC excited at 488 nm. (F) Penetration depths of evanescent field at a different angle of incidence at the core-cladding interface. (G) Mini-TIRF response to blank sample (1× PBS, $n = 5$) on 10 different cartridges.

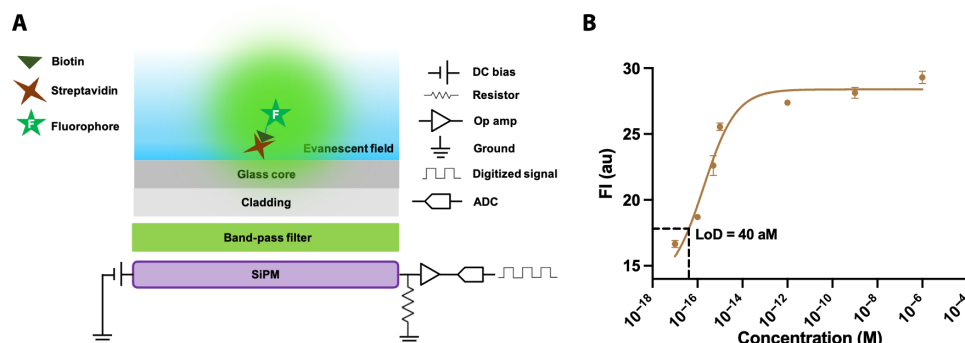


Fig. 5. Detection of biotinylated FITC using mini-TIRF. (A) Schematic showing the excitation of biotinylated FITC bound to surface-immobilized streptavidin by evanescent field. Band-pass filter selectively allows fluorescent emission and stops stray photons from the scattered evanescent field caused by surface-bound molecules. SiPM detects the photons from the fluorescence emission, and an ADC of a microcontroller detects the SiPM signal after amplification. (B) Detection of biotinylated FITC in 1× PBS (pH 7.4) from attomolar to micromolar concentration using mini-TIRF. The LoD was calculated using equation (5).

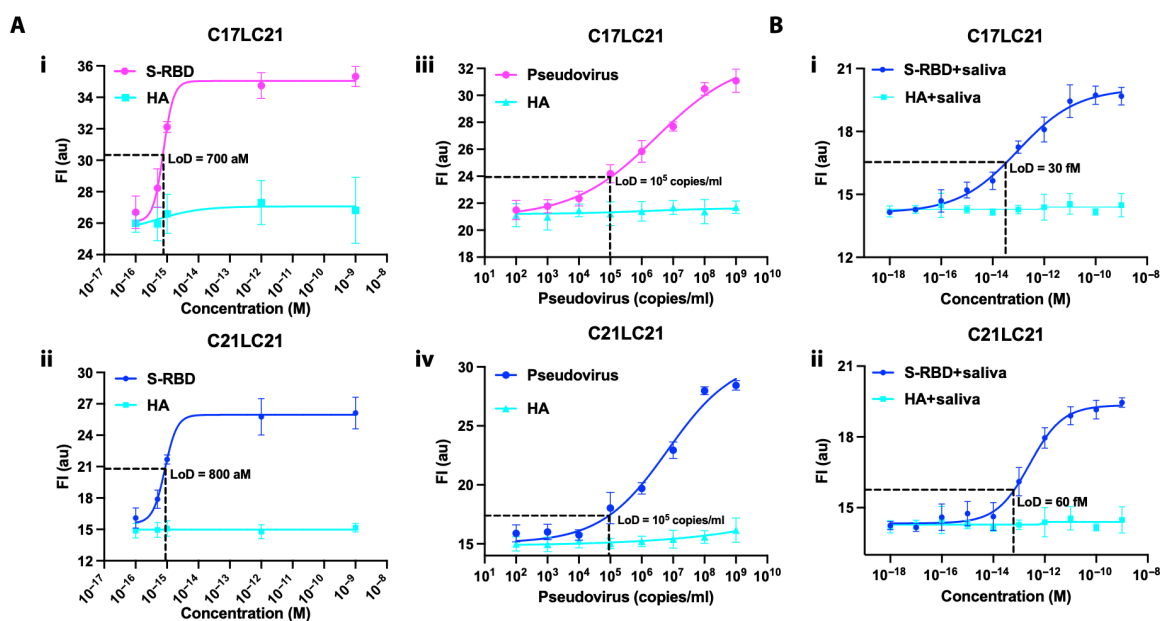


Fig. 6. Detection of S-RBD and pseudotyped SARS-CoV-2 virus particles on mini-TIRF. (A) Detection of the recombinant S-RBD and influenza H3N2 (HA) in 1× PBS by HPLC-purified (i) C17LC21 ($n = 5$) and (ii) C21LC21 ($n = 5$) immobilized on mini-TIRF. Detection of SARS-CoV-2 spike protein bearing pseudovirus and influenza H3N2 (HA) in 1× PBS by HPLC-purified (iii) C17LC21 ($n = 5$) and (iv) C21LC21 ($n = 5$) immobilized on mini-TIRF. (B) Detection of the recombinant S-RBD and influenza H3N2 (HA) in a human saliva sample by HPLC-purified (i) C17LC21 ($n = 5$) and (ii) C21LC21 ($n = 5$) immobilized on mini-TIRF. The LoD was calculated using equation (5).

(pH 7.4) (Fig. 6A, i and ii). Our results demonstrate that the beacon-immobilized mini-TIRF can detect S-RBD with an LoD of nearly 700 aM for C17LC21-Biotin and 800 aM C21LC21-Biotin at low cross-reactivity with HA.

We further measured the fluorescent signal following a 10-min exposure to different copy numbers of SARS-CoV-2 pseudovirus (MyBioSource, #MBS5308351) in a test volume. The peptide beacon-immobilized mini-TIRF demonstrated detection of virus particles with an LoD of nearly 10^5 copies/ml range for both C17LC21-Biotin and C21LC21-Biotin (Fig. 6A, iii and iv).

Detection of S-RBD in a simulated clinical sample

Last, we decided to characterize the response of the beacon-immobilized mini-TIRF in the presence of simulated clinical samples, which were prepared by serially diluting S-RBD in commercially purchased

human saliva (Innovative Research, #IRHUSL5ML). We measured the fluorescent signals from the sensor following a 10-min exposure to different concentrations of S-RBD and HA in human saliva samples. Our results demonstrate that the beacon-immobilized mini-TIRF can detect S-RBD in saliva with an LoD of nearly 30 fM for C17LC21-Biotin and 60 fM for C21LC21-Biotin, as compared to the negative HA control (Fig. 6B, i and ii).

DISCUSSION

In this study, using computational protein modeling tools, we verified and tested a set of molecular beacons that can potentially bind to the S-RBD of SARS-CoV-2 and release a fluorescence signal via FRET, enabling femtomolar detection levels. Later integrating the TIRF microscope and single-photon-sensitive silicon photomultiplier

(SiPM) detector technology, we fabricated and tested mini-TIRF microscopes that detect the fluorescent signal from the surface-bound fluorophores. The final device is portable, low cost, and easy to construct without requiring sophisticated fabrication equipment or facilities. In total, by integrating these peptide beacons within the mini-TIRF, we can detect S-RBD and viral particles with femtomolar sensitivity, thus yielding a rapid, point-of-care diagnostic platform for SARS-CoV-2. Such a diagnostic paradigm is far more efficient than existing RT-PCR assays and potentially more sensitive than antigen-based rapid testing (6, 7).

While our pipeline showcases a potential use case for current deep learning tools, we recognize that the resolution and accuracy of computational protein structure prediction and docking still require further development and testing. Thus, we are continually improving the validation pipeline of molecular beacons using more novel protein folding methods, such as AlphaFold (39), and our progress can be tracked here: <https://doi.org/10.5281/zenodo.6824063>.

Nonetheless, there are many unique opportunities to leverage our platforms further. For example, by fixing the heterodimer motif, the binding loops of molecular beacons can be filled in via protein hallucination (40), using protein folding algorithms such as AlphaFold or EquiDock as verification (39, 41). Moreover, leveraging mini-TIRF technology with immobilized molecular beacons, as developed here, we provide an efficient and ultrasensitive method of detection of fluorescent signals, eliminating costly processing steps of previous diagnostic methods, especially those that require nucleic acid isolation. Together, by using a hybrid approach of protein modeling and novel photonics-based tool development, our design pipeline serves as a powerful platform to fight the continued risk of COVID-19 and future emergent viral threats.

MATERIALS AND METHODS

In silico selection of candidate peptide beacons

The three peptide beacon sequences were folded in the absence of S-RBD using trRosetta. trRosetta is a deep learning tool to predict structures from sequence information. The three peptide beacon sequences were also folded using Rosetta Abinitio folding. Abinitio folding solves the protein structure from sequence through physics-based constraints rather than relying on previously solved structures like trRosetta.

The three peptide beacon sequences were docked against the S-RBD using HDOCK. HDOCK is a protein-protein docking platform that combines ab initio free docking and template-based modeling. The top 100 predictions from HDOCK were analyzed to visualize the structure of peptide beacon sequences in the presence of S-RBD.

Generation of plasmids

pcDNA3-SARS-CoV-2-S-RBD-sfGFP (Addgene, #141184) and pcDNA3-R4-uAb (Addgene, #101800) were obtained as gifts from E. Procko and M. DeLisa, respectively. Peptide beacon sequences were ordered as gBlocks (IDT) and were amplified with overhangs for Gibson Assembly-mediated insertion into linearized pcDNA3-R4-uAb digested with Hind III and Eco RI. Assembled constructs were transformed into 50- μ l NEB Turbo Competent *Escherichia coli* cells and plated onto LB agar supplemented with the appropriate antibiotic for subsequent sequence verification of colonies and plasmid purification.

Cell culture

Human embryonic kidney 293T cells were maintained in Dulbecco's modified Eagle's medium supplemented with penicillin (100 U/ml), streptomycin (100 mg/ml), and 10% fetal bovine serum. RBD-sfGFP (250 ng) and peptide-E3 ligase fusion (250 ng) plasmids were transfected into cells (2×10^5 per well in a 24-well plate) with Lipofectamine 3000 (Invitrogen) in Opti-MEM (Gibco). After 5 days post-transfection, cells were harvested and analyzed on a BD FACSCelesta flow cytometer (BD Biosciences) for GFP fluorescence (488-nm laser excitation, 530/30 filter for detection). Cells expressing GFP were gated, and percent GFP⁺ depletion to the RBD-sfGFP-only control was calculated. All samples were performed in independent transfection duplicates ($n = 2$), and percentage depletion values were averaged.

Peptide synthesis and purification

Beacon peptide sequences can be found in table S1. CxxL [25 μ M, 1 \times PBS (pH 7.4)] was added to C21 [25 μ M, 1 \times PBS (pH 7.4)] and incubated at room temperature for 2 hours for the conjugation reaction between the thiol group of cysteine at the N terminus of CxxL and the maleimide group at the N terminus of C21 (fig. S1A). CxxL + C21 is used to represent the reaction mixture obtained after 2 hours of reaction between CxxL and C21 in 1 \times PBS (pH 7.4) at room temperature. MALDI-TOF mass spectroscopy of CxxL + C21 confirms the presence of CxxLC21 in CxxL + C21 along with CxxL and C21 (fig. S1, B to D). The reaction mixture of CxxL and C21 contains the mixture of individual CxxL, C21, and CxxLC21 after 2 hours of reaction in 1 \times PBS (pH 7.4) at room temperature. Consequently, CxxLC21 from CxxL + C21 was purified using HPLC (Agilent 1100) using a C14 H31 column. HPLC chromatogram of CxxL + C21 contains peaks at a distinct retention time than that of CxxL and C21 in HPLC chromatogram (fig. S1, E to G), which are considered as the fraction containing CxxLC21. The fraction was collected, and MALDI-TOF mass spectroscopy was performed (Microflex LRF, Bruker), confirming the presence of CxxLC21 at a higher concentration than that of CxxL and C21 (fig. S1, H to J). The collected fraction was freeze-dried and used for the detection of S-RBD and HA.

In vitro detection of S-RBD

S-RBD (Abcam, #ab273065) and influenza H3N2 HA (MyBioSource, #MBS5308351) were titrated against purified CxxLC21. S-RBD and HA proteins were serially diluted in 1 \times PBS (pH 7.4) from nanomolar to attomolar concentration. CxxLC21 (2 nM) in 1 \times PBS (pH 7.4) ($n = 3$ or 5) was exposed to different concentrations of the target protein (S-RBD or HA) and incubated for 10 min at room temperature. Fluorescence intensity was subsequently measured using a Tecan Spark well plate reader at excitation and emission wavelength of 480 nm [full width at half maximum (FWHM) = 10 nm] and 525 nm (FWHM = 10 nm), respectively. The fluorescence data were fitted to a sigmoidal 4PL curve in the Prism software. The LoD is estimated from Eq. 5.

Fabrication of mini-TIRF

Within mini-TIRF microscope devices, the collimated laser beam hits the side surface of the planar waveguide at a coupling angle (θ_c) such that the refracted beam within the glass core $n_{\text{core}} = 1.53$ will hit the core-cladding interface at an incident angle (θ_i) greater than the critical angle (θ_{critical}) of the core-cladding pair to make TIR

(Fig. 4A). The cladding is a low-refractive index polymer cladding $n_{\text{cladding}} = 1.34$. The critical angle of the used glass-polymer pair is 61.142° for light having a wavelength of 488 nm, which is calculated using the following Eq. 1. Using Eq. 2, we calculated a range of coupling angles that makes laser beam incident at the core-cladding interface at an angle more than the critical angle. Subsequently, the laser beam propagates along the length of the waveguide bouncing between the top and bottom core-cladding interface making TIR (Fig. 4A). TIR spots are the small areas on the core along the line of propagation of the laser beams, where TIR happens within the core and evanescent field penetrates to the cladding. L_{TIR} and W_{TIR} are the dimensions of the TIR spot along the length and width of the waveguide, which helped us to locate the TIR spots on the core. W_{TIR} is approximately the same as the width of the laser beam falling on the side surface of the waveguide, and L_{TIR} is calculated following Eq. 3. The penetration depth of evanescent waves is the height from the surface after which the intensity of evanescent waves drops by $1/e$ (37%). The penetration depth (d) of the evanescent field was calculated for the range of angles of incidence using Eq. 4. To detect the fluorescence emission from a surface-bound fluorophore within the sample well, a combination of a plano-convex lens, dichroic filter, and SiPM was placed concentrically below the sample well (Fig. 4A). Plano-convex lens collimates the fluorescence emission from the sample well so that the emission incidents on the filter at 0° . The dichroic filter (530 nm; FWHM, 24 nm) specifically allows the fluorescence emission to fall at 0° of incidence while reflecting all the emissions other than the fluorescence emission emitted from the sample well (Fig. 4A). SiPM is a single-photon-sensitive photodetector that was used to detect fluorescence emission. We measured the intensity of fluorescence emission from the amplified SiPM signal using an analog-to-digital converter (ADC) of a microcontroller

$$\theta_{\text{critical}} = \sin^{-1}\left(\frac{n_{\text{cladding}}}{n_{\text{core}}}\right) \quad (1)$$

$$\theta_{\text{C}} = \sin^{-1}\left(n_{\text{core}} \sin\left(\frac{\pi}{2} - \theta_i\right)\right) \quad (2)$$

$$L_{\text{TIR}} = \frac{t_{\text{core}}}{\tan\left(\frac{\pi}{2} - \theta_i\right)} \quad (3)$$

$$d = \frac{\lambda_{\text{excitation}}}{4\pi\sqrt{n_{\text{core}}^2 \sin^2 \theta_i - n_{\text{cladding}}^2}} \quad (4)$$

where the $\lambda_{\text{excitation}}$ is the wavelength of the excitation source.

The computer-aided design model of the cartridge was constructed using SOLIDWORKS software, and the Prusa three-dimensional (3D) printer was used to print the casings of the device (Fig. 4, B and C). The streptavidin-coated glass slide (MicroSurface Inc.) was diced into small chips (length = 25 mm and width = 10 mm) using a dicing saw. The diced glass chip was dip-coated with low-refractive index polymer (Luvantix ADM, #PC-340-HA) and ultraviolet-cured under continuous nitrogen purge. The lower and upper covers were cut out from a 3.175-mm-thick opaque acrylic sheet (Fig. 4, B and C). The visible band-pass filter (530 nm; FWHM, 24 nm; 50 mm by 50 mm) was diced into small pieces using a dicing saw. A SiPM (KETEK, #PM3347-WL PIN) mounted on a polychlorinated biphenyl was assembled with the 3D-printed cartridge along with the diced optical filter and lens keeping them concentric to the TIR spot

within the sample well. A preamplifier (KETEK, #PEVAL-KIT-MCX) and SiPM bias source (KETEK, #SiPM-BIAS SOURCE) were used to amplify the SiPM signal. The 3D-printed white box contains the preamplifier and bias source (fig. S3). On the top surface of the box, there are slots for the laser diode (LD) and SiPM pins to place the cartridge by plugging the LD and SiPM pins, on the bottom of the cartridge, into those slots. An opaque lid was used to provide a light-tight environment room during signal readout to avoid background photons present in the environment (fig. S3D). The amplified signal from the SiPM evaluation kit is acquired through the ADC of a Teensy 3.6 development board at 15-bit resolution with a reference voltage of 3.3 V. The acquired digitized signal was integrated over 1 s, which quantifies the intensity of fluorescence emission falling on the SiPM.

Confirmation of evanescent wave on mini-TIRF

A layer of 1- μm fluorescent microspheres (TetraSpeck) was drop-casted within the sample well, and an additional drop of the microsphere suspension was placed on the microsphere layer. The drop on the microsphere layer was imaged under the confocal microscope. In general, the objective is moved up in the z axis stepwise during z -stack imaging to collect fluorescence signals from different focal planes. The z -stack imaging of the microsphere layer-drop system was performed with mini-TIRF illumination and epi-illumination of the confocal microscope. The z -stack imaging under both illuminations was compared to confirm the presence of evanescent waves in the case of mini-TIRF illumination. Because the evanescent wave is confined within hundreds of nanometers above the surface, under mini-TIRF illumination, only surface-bound microspheres will be excited and emit fluorescence. However, under the epi-illumination mode, microspheres both on the surface and within the drop will be excited by the laser beam. During z -stack imaging, new fluorescent microspheres appeared at subsequent focal planes above the surface under epi-illumination (movie S1). However, in the case of mini-TIRF illumination, a fixed number of fluorescent microspheres appeared at the image plane coinciding with the surface of the core, and the fluorescence from the same microspheres faded gradually when the focal plane moves up above the surface, and eventually, the fluorescence disappeared. Furthermore, no new microspheres appeared at subsequent focal planes above the surface under mini-TIRF illumination (movie S2), which confirms that the illumination within the sample well is caused by the evanescent field.

Detection of biotin-FITC using mini-TIRF

Biotin-FITC (Thermo Fisher Scientific, #22030) was serially diluted in $1\times$ PBS (pH 7.4) from nanomolar to attomolar concentrations. A $10\text{-}\mu\text{l}$ droplet of biotinylated FITC in $1\times$ PBS (pH 7.4) was placed in the sample well and incubated for 30 min at room temperature. Fluorescence intensity was subsequently measured using a mini-TIRF. The fluorescence data were fitted to a sigmoidal 4PL curve in the Prism software. The LoD was estimated from the equation given (Eq. 5).

Detection of S-RBD and SARS-CoV-2 pseudovirus on mini-TIRF

S-RBD, influenza H3N2 HA, and SARS-CoV-2 pseudovirus (10×10^8 copies/ml; MyBioSource, #MBS434278) were used to characterize the response of CxxLC21-Biotin-immobilized mini-TIRF. S-RBD and HA proteins were serially diluted in $1\times$ PBS (pH 7.4) from nanomolar to attomolar concentration. Pseudovirus

was serially diluted in 1× PBS (pH 7.4) from 100 to 10 × 10⁸ copies/ml. Simulated clinical samples were prepared by serially diluting S-RBD in heat-inactivated, commercially purchased human saliva (Innovative Research, #IRHUSL5ML) from nanomolar to attomolar concentrations. The simulated clinical samples were further diluted 10 times in 1× PBS (pH 7.4) before testing with the mini-TIRF. CxxLC21-Biotin (2 nM) in 1× PBS (pH 7.4) was exposed to the streptavidin-coated surface within the sample well and incubated for 60 min at room temperature in the dark. After 60 min, the sample well was washed with 1× PBS several times until no change in fluorescence from the surface-bound peptide beacons after each washing step was observed. A 10-μl droplet of the sample was placed within the sample well and incubated for 10 min in the dark at room temperature. After the incubation period, fluorescence was measured from the mini-TIRF, and data were fitted to a sigmoidal 4PL curve in the Prism software. The LoD is estimated from Eq. 5.

Statistics and reproducibility

All samples were performed in independent duplicates ($n = 2$), triplicates ($n = 3$), or quintuplicates ($n = 5$), as indicated. SD was used to calculate error bars. Statistical analyses were performed using two-tailed Student's t test, using the GraphPad software package. Fluorescence data obtained from the well plate reader and mini-TIRF were fitted to a sigmoidal 4PL curve in the Prism software. The LoD is estimated from the equation given below (42)

$$\text{LoD} = \text{Mean}_{\text{Blank}} + 1.645 \times \text{SD}_{\text{Blank}} + 1.645 \times \text{SD}_{\text{Low}} \quad (5)$$

where Mean_{Blank} is the mean fluorescence intensity of the blank, SD_{Blank} is the SD in the measurement of fluorescent intensity of the blank, and SD_{Low} is the SD in the measurement of fluorescence intensity of a known low-concentration analyte. All fluorescence data are provided in tables S2 to S4.

SUPPLEMENTARY MATERIALS

Supplementary material for this article is available at <https://science.org/doi/10.1126/sciadv.abn2378>

[View/request a protocol for this paper from Bio-protocol.](#)

REFERENCES AND NOTES

- W. Wang, Y. Xu, R. Gao, R. Lu, K. Han, G. Wu, W. Tan, Detection of SARS-CoV-2 in different types of clinical specimens. *JAMA* **323**, 1843–1844 (2020).
- M. Patchesung, K. Jantarug, A. Pattama, K. Aphicho, S. Suraritdechachai, P. Meesawat, K. Sappakhaw, N. Leelahakorn, T. Ruenkam, T. Wongsatit, N. Athipanyasilp, B. Eiamthong, B. Lakkanasirorat, T. Phoodokmai, N. Niljianskul, D. Pakotiprapha, S. Chanarat, A. Homchan, R. Tinikul, P. Kamutira, K. Phiwkaow, S. Soithongcharoen, C. Kantiwiriyanitch, V. Pongsupasa, D. Trisrivirat, J. Jaroensuk, T. Wongnate, S. Maenpuen, P. Chaiyen, S. Kamnerdnakta, J. Swangsri, S. Chuthapisith, Y. Sirivatanauksorn, C. Chaimayo, R. Sutthent, W. Kantakamalakul, J. Joung, A. Ladha, X. Jin, J. S. Gootenberg, O. O. Abudayyeh, F. Zhang, N. Horthongkham, C. Uttamapinant, Clinical validation of a cas13-based assay for the detection of SARS-CoV-2 RNA. *Nat. Biomed. Eng.* **4**, 1140–1149 (2020).
- L. Guo, X. Sun, X. Wang, C. Liang, H. Jiang, Q. Gao, M. Dai, B. Qu, S. Fang, Y. Mao, Y. Chen, G. Feng, Q. Gu, R. H. Wang, Q. Zhou, W. Li, SARS-CoV-2 detection with CRISPR diagnostics. *Cell Discov.* **6**, 34 (2020).
- J. P. Broughton, X. Deng, G. Yu, C. L. Fasching, V. Servellita, J. Singh, X. Miao, J. A. Streithorst, A. Granados, A. Sotomayor-Gonzalez, K. Zorn, A. Gopez, E. Hsu, W. Gu, S. Miller, C. Y. Pan, H. Guevara, D. A. Wadford, J. S. Chen, C. Y. Chiu, CRISPR-cas12-based detection of SARS-CoV-2. *Nat. Biotechnol.* **38**, 870–874 (2020).
- L. Mautner, C.-K. Baillie, H. M. Herold, W. Volkwein, P. Guertler, U. Eberle, N. Ackermann, A. Sing, M. Pavlovic, O. Goerlich, U. Busch, L. Wassill, I. Huber, A. Baiker, Rapid point-of-care detection of SARS-CoV-2 using reverse transcription loop-mediated isothermal amplification (RT-LAMP). *Virol. J.* **17**, 160 (2020).
- B. D. Kevadiya, J. Machhi, J. Herskovitz, M. D. Oleynikov, W. R. Blomberg, N. Bajwa, D. Soni, S. Das, M. Hasan, M. Patel, A. M. Senan, S. Gorantla, J. E. McMillan, B. Edagwa, R. Eisenberg, C. B. Gurumurthy, S. P. M. Reid, C. Punyadeera, L. Chang, H. E. Gendelman, Diagnostics for SARS-CoV-2 infections. *Nat. Mater.* **20**, 593–605 (2021).
- S. A. Bustin, T. Nolan, RT-qPCR testing of SARS-CoV-2: A primer. *Int. J. Mol. Sci.* **21**, 3004 (2020).
- V. M. Corman, V. C. Haage, T. Bleicker, M. L. Schmidt, B. Mühlemann, M. Zuchowski, W. K. Jo, P. Tscheak, E. Möncke-Buchner, M. A. Müller, A. Krumbholz, J. F. Drexler, C. Drosten, Comparison of seven commercial SARS-CoV-2 rapid point-of-care antigen tests: A single-centre laboratory evaluation study. *Lancet Microbe* **2**, e311–e319 (2021).
- L. Bokelmann, O. Nickel, T. Maricic, S. Pääbo, M. Meyer, S. Borte, S. Riesenberger, Point-of-care bulk testing for SARS-CoV-2 by combining hybridization capture with improved colorimetric LAMP. *Nat. Commun.* **12**, 1467 (2021).
- G. Xun, S. T. Lane, V. A. Petrov, B. E. Pepa, H. Zhao, A rapid, accurate, scalable, and portable testing system for COVID-19 diagnosis. *Nat. Commun.* **12**, 2905 (2021).
- X. Ding, K. Yin, Z. Li, R. V. Lalla, E. Ballesteros, M. M. Sfeir, C. Liu, Ultrasensitive and visual detection of SARS-CoV-2 using all-in-one dual CRISPR-cas12a assay. *Nat. Commun.* **11**, 4711 (2020).
- M. J. Kellner, J. G. Koob, J. S. Gootenberg, O. O. Abudayyeh, F. Zhang, SHERLOCK: Nucleic acid detection with CRISPR nucleases. *Nat. Protoc.* **14**, 2986–3012 (2019).
- T. Wazawa, M. Ueda, Total internal reflection fluorescence microscopy in single molecule nanobioscience. *Adv. Biochem. Eng. Biotechnol.* **95**, 77–106 (2005).
- Y. Miyana, S. Matsuoka, M. Ueda, Single-molecule imaging techniques to visualize chemotactic signaling events on the membrane of living *Dictyostelium* cells, in *Chemotaxis*, T. Jin, D. Hereld, Eds. (Springer, 2009), pp. 417–435.
- M. Tokunaga, K. Kitamura, K. Saito, A. H. Iwane, T. Yanagida, Single molecule imaging of fluorophores and enzymatic reactions achieved by objective-type total internal reflection fluorescence microscopy. *Biochem. Biophys. Res. Commun.* **235**, 47–53 (1997).
- F. Luo, G. Qin, T. Xia, X. Fang, Single-molecule imaging of protein interactions and dynamics. *Annu. Rev. Anal. Chem.* **13**, 337–361 (2020).
- S.-L. Ho, H. M. Chan, A. W. Y. Ha, R. N. S. Wong, H. W. Li, Direct quantification of circulating mirnas in different stages of nasopharyngeal cancerous serum samples in single molecule level with total internal reflection fluorescence microscopy. *Anal. Chem.* **86**, 9880–9886 (2014).
- S. L. Reck-Peterson, N. D. Derr, N. Stuurman, Imaging single molecules using total internal reflection fluorescence microscopy (TIRFM). *Cold Spring Harb. Protocols* **2010**, pdb.top73 (2010).
- H.-M. Chan, L. S. Chan, R. N. S. Wong, H. W. Li, Direct quantification of single-molecules of microRNA by total internal reflection fluorescence microscopy. *Anal. Chem.* **82**, 6911–6918 (2010).
- S. H. Kang, M. R. Shortreed, E. S. Yeung, Real-time dynamics of single-dna molecules undergoing adsorption and desorption at liquid–solid interfaces. *Anal. Chem.* **73**, 1091–1099 (2001).
- G. Yao, X. Fang, H. Yokota, T. Yanagida, W. Tan, Monitoring molecular beacon dna probe hybridization at the single-molecule level. *Chemistry* **9**, 5686–5692 (2003).
- T. Wazawa, M. Ueda, Total internal reflection fluorescence microscopy in single molecule nanobioscience, in *Microscopy Techniques* (Springer, 2005), pp. 77–106; <https://doi.org/10.1007/b102211>.
- B. R. Schudel, M. Tanyeri, A. Mukherjee, C. M. Schroeder, P. J. A. Kenis, Multiplexed detection of nucleic acids in a combinatorial screening chip. *Lab Chip* **11**, 1916–1923 (2011).
- S.-J. Jeong, S.-K. Park, J.-K. Chang, S.-H. Kang, Ultra-sensitive real-time single-DNA molecules detection at a fused-silica/water interface using TIRFM technique. *Bull. Korean Chem. Soc.* **26**, 979–982 (2005).
- S. Ramachandran, D. A. Cohen, A. P. Quist, R. Lal, High performance, LED powered, waveguide based total internal reflection microscopy. *Sci. Rep.* **3**, 2133 (2013).
- V. Pandey, S. Gupta, R. Elangovan, Compact 3D printed module for fluorescence and label-free imaging using evanescent excitation. *Methods Appl. Fluoresc.* **6**, 015007 (2017).
- B. Agnarsson, M. Mapar, M. Sjöberg, M. Alizadehheidari, F. Höök, Low-temperature fabrication and characterization of a symmetric hybrid organic–inorganic slab waveguide for evanescent light microscopy. *Nano Futures* **2**, 025007 (2018).
- A. Archetti, E. Glushkov, C. Sieben, A. Stroganov, A. Radenovic, S. Manley, Waveguide-PAINT offers an open platform for large field-of-view super-resolution imaging. *Nat. Commun.* **10**, 1267 (2019).
- Y. Minagawa, H. Ueno, K. V. Tabata, H. Noji, Mobile imaging platform for digital influenza virus counting. *Lab Chip* **19**, 2678–2687 (2019).
- A. N. Gortari, S. Bouchoule, E. Cambril, A. Cattoni, L. Hauke, J. Enderlein, F. Rehfeldt, A. Yacomotti, Metasurface-based total internal reflection microscopy. *Biomed. Opt. Express* **11**, 1967–1976 (2020).
- I. L. Medintz, N. Hildebrandt, *FRET-Förster Resonance Energy Transfer: From Theory to Applications* (John Wiley & Sons, 2013).

32. C. Mueller, T. N. Grossmann, Coiled-coil peptide beacon: A tunable conformational switch for protein detection. *Angew. Chem. Int. Ed.* **57**, 17079–17083 (2018).
33. P. Chatterjee, M. Ponnampati, C. Kramme, A. M. Plesa, G. M. Church, J. M. Jacobson, Targeted intracellular degradation of SARS-CoV-2 via computationally optimized peptide fusions. *Commun. Biol.* **3**, 715 (2020).
34. J. Yang, I. Anishchenko, H. Park, Z. Peng, S. Ovchinnikov, D. Baker, Improved protein structure prediction using predicted interresidue orientations. *Proc. Natl. Acad. Sci. U.S.A.* **117**, 1496–1503 (2020).
35. R. Bonneau, J. Tsai, I. Ruczinski, D. Chivian, C. Rohl, C. E. M. Strauss, D. Baker, Rosetta in CASP4: Progress in ab initio protein structure prediction. *Proteins* **45**, 119–126 (2001).
36. Y. Yan, H. Tao, J. He, S. Y. Huang, The HDock server for integrated protein–protein docking. *Nat. Protoc.* **15**, 1829–1852 (2020).
37. C. J. Russell, M. Hu, F. A. Okda, Influenza hemagglutinin protein stability, activation, and pandemic risk. *Trends Microbiol.* **26**, 841–853 (2018).
38. Y. Xiang, S. Nambulli, Z. Xiao, H. Liu, Z. Sang, W. P. Duprex, D. Schneidman-Duhovny, C. Zhang, Y. Shi, Versatile and multivalent nanobodies efficiently neutralize SARS-CoV-2. *Science* **370**, 1479–1484 (2020).
39. J. Jumper, R. Evans, A. Pritzel, T. Green, M. Figurnov, O. Ronneberger, K. Tunyasuvunakool, R. Bates, A. Žídek, A. Potapenko, A. Bridgland, C. Meyer, S. A. A. Kohl, A. J. Ballard, A. Cowie, B. Romera-Paredes, S. Nikolov, R. Jain, J. Adler, T. Back, S. Petersen, D. Reiman, E. Clancy, M. Zielinski, M. Steinegger, M. Pacholska, T. Berghammer, S. Bodenstein, D. Silver, O. Vinyals, A. W. Senior, K. Kavukcuoglu, P. Kohli, D. Hassabis, Highly accurate protein structure prediction with AlphaFold. *Nature* **596**, 583–589 (2021).
40. I. Anishchenko, S. J. Pellock, T. M. Chidyausiku, T. A. Ramelot, S. Ovchinnikov, J. Hao, K. Bafna, C. Norn, A. Kang, A. K. Bera, F. DiMaio, L. Carter, C. M. Chow, G. T. Montelione, D. Baker, De novo protein design by deep network hallucination. *Nature* **600**, 547–552 (2021).
41. O.-E. Ganea, O.-E. Ganea, X. Huang, C. Bunne, Y. Bian, R. Barzilay, T. Jaakkola, A. Krause, Independent se(3)-equivariant models for end-to-end rigid protein docking. arXiv: 2111.07786 [cs.AI] (15 November 2021).
42. R. C. May, H. Chu, J. G. Ibrahim, M. G. Hudgens, A. C. Lees, D. M. Margolis, Change-point models to estimate the limit of detection. *Stat. Med.* **32**, 4995–5007 (2013).

Acknowledgments: We thank N. Gershenfeld, S. Zhang, and E. S. Boyden for shared laboratory equipment and T. Stan for technical assistance. **Funding:** This work was supported by the consortia of sponsors of the MIT Media Lab and the MIT Center for Bits and Atoms and by J. and J. Wertheimer. **Author contributions:** S.P.T. conducted peptide beacon purification, synthesis, and in vitro characterization. M.P. conducted computational design and docking protocols and performed experiments. S.B. assisted with computational docking protocols. P.C. designed and built plasmid constructs, performed degradation assays, and conducted data analysis. S.P.T. designed, fabricated, and characterized mini-TIRF microscopes, with input from P.C. and J.J. P.C., S.P.T., and M.P. wrote the manuscript. P.C. and J.J. supervised the project. **Competing interests:** P.C., M.P., S.P.T., and J.J. are listed as inventors for U.S. Provisional Patent Application 63/182,537 entitled “Peptide Based Probes For the Detection of SARS-CoV-2.” **Data and materials availability:** All data needed to evaluate the conclusions in the paper are present in the paper and/or the Supplementary Materials. All source computational and experimental data files can be accessed at <https://doi.org/10.5281/zenodo.6824063>.

Submitted 12 November 2021

Accepted 13 July 2022

Published 24 August 2022

10.1126/sciadv.abn2378